The Nontraditional Coriolis Terms and Tropical Convective Clouds

MATTHEW R. IGEL[a] AND JOSEPH A. BIELLO[b]

[a] *Department of Land, Air and Water Resources, University of California, Davis, Davis, California;* [b] *Department of Mathematics, University of California, Davis, Davis, California*

(Manuscript received 24 January 2020, in final form 27 August 2020)

ABSTRACT: The full, three-dimensional Coriolis force includes the familiar sine-of-latitude terms as well as frequently dropped cosine-of-latitude terms [nontraditional Coriolis terms (NCT)]. The latter are often ignored because they couple the zonal and vertical momentum equations that in the large-scale limit of weak vertical velocity are considered insignificant almost everywhere. Here, we ask whether equatorial mesoscale clouds that fall outside the large-scale limit are affected by the NCT. A simple scaling indicates that a Lagrangian parcel convecting at $10\,\mathrm{m\,s^{-1}}$ through the depth of the troposphere should be deflected over 2 km to the west. To understand the real impact of NCT, we develop a mathematical framework that describes an azimuthally symmetric convective circulation with an analytical expression for an incompressible poloidal flow. Because the model incorporates the full three-dimensional flow associated with convection, it uniquely predicts not only the westward tilt of clouds but also a meridional diffluence of western cloud outflow. To test these predictions, we perform a set of cloud-resolving simulations whose results show preferential lifting of surface parcels with positive zonal momentum and zonal asymmetry in convective strength. RCE simulations show changes to the organization of coherent precipitation regions and a decrease in mean convective intensity of approximately $2\,\mathrm{m\,s^{-1}}$ above the freezing level. An additional pair of dry cloud-resolving simulations designed to mimic the steady-state flow of the model show maximum perturbations to the upper-level zonal flow of $8\,\mathrm{m\,s^{-1}}$. Together, the numerical and analytic results suggest the NCT consequentially alter equatorial mesoscale convective circulations and should be considered in conceptual models.

KEYWORDS: Atmospheric circulation; Oscillations; Subsidence; Cloud resolving models; Clouds

1. Introduction

In a typical introductory atmospheric dynamics class, students often derive the full form of the Coriolis force—the apparent force introduced by formulating our equations of motion in a noninertial reference frame (de Coriolis 1835; Poisson 1838) attached to the rotating Earth. In three dimensions, in a rotating frame of reference, the momentum equations for an inviscid fluid are

$$\frac{Du}{Dt}+\frac{\partial p}{\partial x}=2\Omega_0\sin(\phi)v-\underline{2\Omega_0\cos(\phi)w}\,, \tag{1}$$

$$\frac{Dv}{Dt}+\frac{\partial p}{\partial y}=-2\Omega_0\sin(\phi)u\,, \tag{2}$$

$$\frac{Dw}{Dt}+\frac{\partial p}{\partial z}=\underline{2\Omega_0\cos(\phi)u}+B\,. \tag{3}$$

In (1)–(3), u, v, and w are the vector components of the wind, Ω_0 is the rotation rate of Earth, ϕ is the latitude, and B is the reduced gravity. The pressure divided by the mass density is p; in the theory of incompressible flows, this quantity is referred to as the pressure, and we will continue with that convention throughout the paper.

To specify the pressure, we require another equation. When the Mach number of the flow is small–for example, at convective scales in the atmosphere–acoustic waves travel quickly, and the flow can be described through either the anelastic or incompressible approximation. We will use the incompressible approximation in what follows,

$$\frac{\partial u}{\partial x}+\frac{\partial v}{\partial y}+\frac{\partial w}{\partial z}=0\,, \tag{4}$$

although the anelastic constraint would give similar results but in pressure coordinates.

Equations (1)–(4) describe the motion of an ideal fluid under the "full Coriolis force." In an effort to meaningfully simplify the standard equations of motion, we often use scaling arguments, which suggest that, in typical midlatitude conditions, the underlined term on the right-hand side (rhs) of (1) is much smaller than the first, and so can be neglected. We then note that the underlined term on the rhs of (3) is much smaller than the leading order vertical accelerations, gravity and the pressure gradient force. These assumptions lead to the so-called traditional approximation. For standard, synoptic, midlatitude meteorology, the traditional approximation does not introduce any major errors. However, at or near the equator, this approximation is less accurate owing to the relative largeness of $\cos(\phi)$ to $\sin(\phi)$, all other magnitudes being equal. The underlined terms in (1)–(3) are sometimes called the "nontraditional Coriolis terms" (NCT) being derived from the "nontraditional approximation."

Of course, we are not the first to discuss the form or impact of the NCT. The NCT are commonly considered in hydrodynamic flows of deep-atmosphere planets (Savonije and Papaloizou 1997; Ogilvie and Lin 2004; Dintrans et al. 1999) and sometimes on terrestrial ocean dynamics (Denbo and Skyllingstad 1996; Marshall and Schott 1999). Their effect

Corresponding author: Matthew R. Igel, migel@ucdavis.edu

DOI: 10.1175/JAS-D-20-0024.1

on the terrestrial atmosphere is less commonly considered although reasonably well understood in some contexts. Hayashi and Itoh (2012) examined the response to an MJO-like equatorial diabatic heating forced by the NCT. Ong and Roundy (2019) recently examined the response of equatorial synoptic flows to the NCT in a simplified model and separately argued for their inclusion when calculating a meaningful geopotential (Ong and Roundy 2020). Tort and Dubos (2014) developed a shallow atmosphere model with the complete Coriolis force. What these papers all have in common, besides a near universal message not to ignore the NCT, is a limited range of length and time scales of consideration; below the synoptic scale in the atmosphere, the NCT have received little systematic attention with two notable exceptions. LeMone, in her famous paper analyzing (tropical) convective momentum transport observed in a squall line in GATE (LeMone 1983), concludes that in the case examined ''Earth's rotation must be accounted for via [NCT]'' when considering momentum transport as its effect is at least second order. Liang and Chan (2005) examine the effect of NCT on a hurricane and conclude that it can yield asymmetric precipitation patterns, perturbations to storm motion and, as we will, vertical vorticity derived from vertical flow.

In this paper, we ask a simple question about the NCT: what are their impact on three-dimensional tropical mesoscale convective circulations? Part of the motivation for asking this question is practical. For example, the Weather Research and Forecasting (WRF) Model documentation (Skamarock et al. 2008, p. 11) states that for a standard Cartesian grid, the accelerations due to the NCT should be set to zero.[1] But if the effect of the NCT on the kinds of cloud-resolving simulations for which WRF was designed is consequential, WRF users may need to consider the impact of these ignored terms. Cloud Model 1 (CM1) (Bryan and Fritsch 2002) also assumes the NCT are zero (as of version 19.2). The Regional Atmospheric Modeling System (RAMS; Cotton et al. 2003; Saleeby and Cotton 2008) does not include the NCT. The Nonhydrostatic Icosahedral Atmospheric Model (NICAM) (Satoh et al. 2010) *does* include these terms and a version of the fifth-generation PSU–NCAR Mesoscale Model (MM5) (Liang and Chan 2005) does as well—so their exclusion is not universal among cloud-resolving models. Furthermore, it has been argued through a normal mode analysis of the NCT in a compressible, stratified flow that as grid spacing shrinks in global models, NCT should be added there as well (Kasahara 2003).

That being said, we are more generally motivated by a suspicion that the NCT may play an underappreciated role in shaping the evolution of equatorial convective circulations and the resultant morphology of convection. In the preamble to their review of the impact of the NCT on geophysical flows, Gerkema et al. (2008) lamented that,''[as] the interest in [NCT] has waxed and waned repeatedly, the literature is scattered, and much of it has slipped into oblivion.'' Therefore, we think it is plausible that the NCT has been unintentionally ignored at the atmospheric mesoscales.

To answer our motivating question, we rely on cloud-resolving modeling and analytic results. These are organized as follows. In section 2, we examine the equatorial scales of motion implied by the NCT. In section 3, we develop an analytic model for the effect of the NCT on closed equatorial circulations. This analytic model uses an important intuition–acoustic waves travel much more quickly than convective flows, so the atmosphere in the vicinity of a convective flow behaves incompressibly (more accurately, anelastically). Pressure in incompressible flows, is determined diagnostically through the Leray projection. Using the Leray projection, we explicitly describe the force on a model convective flow. The mathematics works out extremely simply and shows one component of the force (we call it the Coriolis Rotation term) to be proportional to the sine of the longitude, which drives the traditional cyclonic/anticyclonic motion associated with convection. The second component of the force is proportional to the cosine of the latitude, is strongest in the tropics, and is, therefore, the primary effect of the NCT. This Coriolis Shear force, as we call it, is systematically present in any vertical convective circulation, is westward in the ascending part of a convective flow, and diffluent in western outflow. In section 4, we calculate the exact NCT and pressure resulting from an analytic expression for a model poloidal convective circulation, the DoNUT model. In section 5, we numerically simulate the impact of the NCT in two cases: one case will show the asymmetric effect zonal velocity has on convective motions and the other will show the effect of the NCT on the statistics of clouds and precipitation. Finally, we test this new analytic model with a pair of steady-state simulations designed to mimic the analytic model.

2. Exploratory results

a. *Inertial circles*

As a suggestive practice, we examine the nature of inertial circles induced by the NCT at the equator. If one considers an air parcel of always-neutral buoyancy that instantaneously adjusts to the local pressure, and neglecting the spatial variations in velocity, then we can compute the classical inertial circles associated with the Coriolis force using (1)–(3). The resulting velocity field is $[u(t), v(t), w(t)] = V_0[\cos(2\Omega_0 t), -\sin(\phi)\sin(2\Omega_0 t), \cos(\phi)\sin(2\Omega_0 t)]$, where V_0 is the initial (zonal) speed of the parcel. The dots in Fig. 1 mark the path of an initially slowly eastward-moving $[u(0) = 1\,\mathrm{m\,s^{-1}}, w(0) = 0\,\mathrm{m\,s^{-1}}]$ parcel at the equator ($\phi = 0$). Over the course of 12 h, the parcel traces out a circle and returns to its initial location. The parcel maintains its initial speed throughout the oscillation. In an idealized sense, this oscillation may be imaged as a simple Taylor column aligned with the rotation axis of the planet, which at the equator is perpendicular (i.e., into the page) to the local vertical (Gerkema et al. 2008; Busse 1976).

The diamonds in Fig. 1 show the evolution of a westward moving $[u(0) = -1\,\mathrm{m\,s^{-1}}, w(0) = 0\,\mathrm{m\,s^{-1}}]$ parcel initially 1 km

[1] The underlined terms on the rhs of (1) and (3) are listed in that documentation as ''curvature terms'' instead of ''Coriolis terms.'' In a broad sense, this is merely a semantic choice by the document's authors, but we would argue against this choice given the appearance of Ω in these terms.

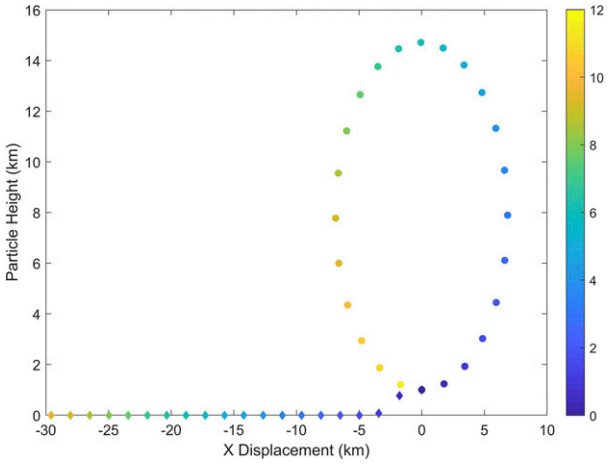

FIG. 1. Illustration of the evolution of a pair of arbitrary neutral air parcels under the influence of the nontraditional Coriolis terms. Marked locations indicate the evolution in space. Colors represent the evolution in time (h; colors lighten as time increases). Circles show a parcel with $U(0) = 1\,\mathrm{m\,s^{-1}}$. Diamonds show a parcel with $U(0) = 1\,\mathrm{m\,s^{-1}}$.

above the surface. This parcel has the same speed as the first example parcel but initially travels in the opposite direction. In this case, the parcel descends until it reaches the surface. At that time, its vertical momentum is transferred to the surface (by construction in our simple example), but its zonal momentum is unaffected. The parcel then skids along the surface with constant momentum thereafter. Thus the behavior of two parcels with identical initial properties, except for the sign of their zonal velocity, is very different when influenced by the NCT and subject to a rigid surface. These examples are contrived and do not include all kinds of real world complexity inherent in parcel motion. That being said, the point they make well is that the NCT have the potential to act asymmetrically because of the confinement of flow in the vertical plane by a rigid surface (and semi-impermeable tropopause).

b. *Simple scaling*

Next, we will test whether the NCT may be nonnegligible at the mesoscale. Before doing so, we will note that we present a stricter scaling in section 4a. The discussion herein is motivational in the sense that it incorporates only parcel thinking, which is intentionally simplistic, and provides only a sense of absolute magnitudes, which must be prejudged in the absence of magnitudes from other forces.

The zonal displacement due to a constant acceleration and zero initial velocity in the zonal direction over a period Δt is, of course,

$$\Delta X = \frac{1}{2}\frac{Du}{Dt}\Delta t^2. \tag{5}$$

If an arbitrary parcel ascends with constant vertical wind speed W_0 over a depth of atmosphere H, then

$$\Delta X = -\Omega_0 \cos(\phi)\frac{H^2}{W_0}. \tag{6}$$

Equation (6) suggests that a zonal displacement of an ascending air parcel depends on the square of the depth of the ascent and inversely on the velocity. We will consider two cases relevant to the tropical atmosphere. The first is of a convecting, cloudy parcel. In this case, $H = 18\,\mathrm{km}$ and $W_0 = 10\,\mathrm{m\,s^{-1}}$. This implies $\Delta X = -2.4\,\mathrm{km}$. Taken literally, this would suggest that up to 2.4 km of the lateral deflection of a cloudy parcel is due purely to Coriolis acceleration. This deflection would mean that convection is not upright but rather tilted at 7.5° with the vertical toward the west.

The second case is one of a subsiding, clear air parcel. In this case, $H = 18\,\mathrm{km}$ and $W_0 = -0.10\,\mathrm{m\,s^{-1}}$. This implies $\Delta X = 240\,\mathrm{km}$. Because of the inverse dependence of the displacement on the magnitude of W_0, the slowly subsiding parcel is displaced more than the relatively quickly convecting parcel. While the lateral displacement of clear air is likely of little direct meteorological consequence, we point out the fate of a forced subsiding parcel because later we will couple convective updrafts to slow compensating subsidence.

The change in speed of a parcel ascending over a depth of atmosphere is

$$\Delta U = -2\Omega_0 \cos(\phi)H. \tag{7}$$

Equation (7) shows that unlike for the displacement of a parcel, the final velocity does not depend on vertical velocity such that ascending and descending parcels gain the same speed, although they are in opposite directions. The zonal velocity of a parcel that ascends through the depth of the tropical troposphere is accelerated by $2.6\,\mathrm{m\,s^{-1}}$ toward the west. Cumulatively, these scales suggest the NCT likely cannot be ignored when considering convection.

3. Effect of the nontraditional Coriolis terms on a general poloidal circulation

The simple scaling in section 2b is convenient yet fundamentally flawed as it employs simple "parcel" thinking. Real convection occurs in a continuous fluid, which means air movement causes pressure perturbations. It is our supposition that even subtle indirect effects of the NCT on the pressure field will be consequential to the complicated mesoscale evolution of convection. Not only will it result in behavior different than the simple scaling indicates in the vertical–zonal plane, but it will also have the potential to introduce meridional flow since the pressure is a nonlocal function of the flow velocity.

As far as the authors are aware, there is no simple mathematical framework incorporating the NCT into the kind of mesoscale convective circulations in which we are interested. So, we now introduce one.

In this section we describe analytically and explicitly the effect of the Coriolis force on an axisymmetric poloidal flow that we envision to be a basic convective circulation. Our first insight is to consider a generic poloidal circulation and compute the total Coriolis force ($\mathbf{F}_{\mathrm{Total}} = -2\boldsymbol{\Omega} \times \mathbf{u}$) experienced by this flow. In general, the total Coriolis force has a net divergence, which, in turn, would force a divergence in the velocity field.

Our second insight is that as long as the Mach number of the convective flow is not large, then sound waves adjust the

pressure in the fluid so that the actual convective circulation is incompressible (or anelastic, but as was noted above, this difference is a matter of details of the computation). This adjustment occurs on the travel time of sound waves, which is very fast compared to the travel time of the flow. In fact, in an incompressible flow the pressure adjusts instantaneously in order to establish a net force that is nondivergent. Therefore, to consider an incompressible flow means that we must restrict attention to the nondivergent component of the force acting on these flows. Thus we define the *net* Coriolis force to be the nondivergent part of the *total* Coriolis force, and we will make this definition mathematically explicit below. For nondivergent velocity fields (incompressible flows), the pressure is determined from the velocity field by inverting a Laplacian through the well-known Leray projection.

The net nondivergent Coriolis force is the sum of the total Coriolis force and the pressure gradient required to maintain a nondivergent force, $\mathbf{F}_{\text{Net}} = -2\boldsymbol{\Omega} \times \mathbf{u} - \nabla p$. Instead of providing an exact solution for the circulation, the Leray projection shows how, for any prescribed circulation, the strength and direction of the net Coriolis force depends on the local flow speed, and how the traditional and nontraditional net Coriolis forces depend on the latitude of the circulation.

Although we will work on an f plane, which means that we neglect the variation of the Coriolis force in our convective scales, we retain the latitudinal dependence of the Coriolis parameter so that we can describe the different effects of the net Coriolis force at different latitudes. Our analysis yields two structurally different net forces, which the Coriolis force induces on a poloidal convective circulation, neither of which has any component in the vertical direction:

1) A toroidal force that is cyclonic in the axially convergent region of the circulation and anticyclonic in the axially divergent region of the circulation. Its strength is proportional to the *sine* of the latitude, and thereby vanishes at the equator and is maximal at the poles. This is the effect of the traditional Coriolis force, which induces a cyclonic/anticyclonic first baroclinic structure.
2) A force that is in the horizontal plane, having a dipolar, diffluent structure around the center of convection. It acts westward in the center of a convective updraft, recirculates poloidally away from the center, is maximal at the point of maximum vertical velocity, and varies as the *cosine* of latitude. These NCT effects are most pronounced at the equator, induce westward tilts in convective updrafts, and force diffluence in western outflow.

Although the derivation of the Coriolis force is straightforward, readers who wish to skip the details may proceed to either sections 5 or 6.

a. The equations for the net Coriolis force

Consider the incompressible Euler equations (in vector form) in a stratified fluid in the presence of rotation (modeled on an f plane),

$$\frac{\partial \mathbf{u}}{\partial t} + \mathbf{u} \cdot \nabla \mathbf{u} + \nabla p + 2\boldsymbol{\Omega} \times \mathbf{u} = B\hat{\mathbf{k}}, \tag{8}$$

$$\nabla \cdot \mathbf{u} = 0, \tag{9}$$

where

$$\boldsymbol{\Omega} = \Omega_0[\cos(\phi)\hat{\mathbf{j}} + \sin(\phi)\hat{\mathbf{k}}], \tag{10}$$

and $\hat{\mathbf{i}}$, $\hat{\mathbf{j}}$, and $\hat{\mathbf{k}}$ are the unit vectors in the local eastward, northward, and upward directions, respectively. The other symbols are the same as described in the previous sections. Equations (8) and (9) are the vector form of (1)–(4), and thereby contain both traditional and nontraditional Coriolis terms. The anelastic generalization of these equations would replace (9) with $\nabla \cdot [\rho(z)\mathbf{u}] = 0$, where $\rho(z)$ is a prescribed density profile. While the details of the computation would change for the anelastic case, the principle of the Leray projection would remain.

The Leray projection provides the algorithm for determining the pressure from a force and circulation, thereby constructing a net, nondivergent force field required to maintain a nondivergent flow $\mathbf{u}$. By taking the divergence of (8) and substituting the time derivative of (9), the pressure can be determined by the inversion of the Laplacian:

$$\nabla^2 p = \nabla \cdot [B\hat{\mathbf{k}} - 2\boldsymbol{\Omega} \times \mathbf{u} - \mathbf{u} \cdot \nabla \mathbf{u}], \tag{11}$$

and thereby contains components due to buoyancy, the Coriolis force, and the fluid inertia, respectively. The boundary conditions for the pressure are determined by the boundary conditions for the flow. On a rigid boundary, the velocity field satisfies

$$\mathbf{u} \cdot \hat{\mathbf{n}} = 0, \tag{12}$$

where $\hat{\mathbf{n}}$ is the unit normal on the boundary. Taking the dot product of (8) with $\hat{\mathbf{n}}$, evaluating it on a rigid boundary, and using (12) yield a Neumann boundary condition for the pressure on the boundary:

$$\nabla p \cdot \hat{\mathbf{n}} = \hat{\mathbf{n}} \cdot [B\hat{\mathbf{k}} - 2\boldsymbol{\Omega} \times \mathbf{u} - \mathbf{u} \cdot \nabla \mathbf{u}]. \tag{13}$$

This is simply the mathematical expression for the balance of normal forces on a rigid boundary. Since the flow cannot penetrate a rigid boundary, the total normal force due to buoyancy, Coriolis, and fluid inertia must be balanced by the normal pressure gradient at that boundary.

On a free boundary, the boundary condition is simply continuity of pressure. In the atmosphere, we will consider a rigid lower boundary (which defines $z = 0$) and decay of pressure as $|\mathbf{x}| \to \infty$.

The question we ask is, when considered at a fixed latitude and on scales appropriate to convective clouds, what is the *net* effect of *only* the Coriolis force on an idealized, axially symmetric, poloidal circulation. We leave to future work the thorough discussion of the effect of the buoyancy, $B\hat{\mathbf{k}}$, and inertia terms, $\mathbf{u} \cdot \nabla \mathbf{u}$, although the latter are briefly considered in section 4a. Therefore, we must solve for *the net Coriolis force* that results after the Leray projection, since in an incompressible flow, the pressure adjusts instantaneously to maintain the nondivergent constraint. To solve this problem involves projecting out the portion of the Coriolis force, which contains divergence. Defining the net Coriolis force as

$$\mathbf{F} = -2\boldsymbol{\Omega} \times \mathbf{u} - \nabla p_C, \tag{14}$$

where p_C, which we call the Coriolis pressure, is determined by requiring $\mathbf{F}$ to be nondivergent:

$$\nabla \cdot \mathbf{F} = 0 \quad \Rightarrow \quad \nabla^2 p_C = -2\nabla \cdot [\boldsymbol{\Omega} \times \mathbf{u}]. \tag{15}$$

The Neumann boundary condition on p_C results from requiring that the normal component of the net force $\mathbf{F} \cdot \hat{\mathbf{n}}$ equals zero on $z = 0$:

$$\frac{\partial p_C}{\partial z} = -2\hat{\mathbf{k}} \cdot (\boldsymbol{\Omega} \times \mathbf{u}) \quad \text{on} \quad z = 0. \tag{16}$$

Since the velocity field decays to zero far from the origin, the Coriolis pressure (which results from the inversion of the three-dimensional Laplacian) limits to a constant far from the origin–and without loss of generality we can set that constant to zero. Any environmental pressure gradient is external to the Leray projection.

b. Computing the Coriolis pressure

Now we construct the Coriolis pressure in $(x, y) \in \mathbf{R}^2$, $z \geq 0$. The Coriolis pressure is the portion of the total pressure field arising from the Coriolis force acting on the velocity field of concern, in our case a poloidal flow that satisfies (15) and boundary conditions (16). To simplify the right-hand side of (15) we use the vector identity $\nabla \cdot [\boldsymbol{\Omega} \times \mathbf{u}] = (\nabla \times \boldsymbol{\Omega}) \cdot \mathbf{u} - (\nabla \times \mathbf{u}) \cdot \boldsymbol{\Omega}$. The rotation vector is constant and the vorticity is defined as the curl of the velocity field $\boldsymbol{\omega} = \nabla \times \mathbf{u}$ so (15) becomes

$$\nabla^2 p_C = 2\boldsymbol{\Omega} \cdot \boldsymbol{\omega}. \tag{17}$$

In the following, we will show that, for axially symmetric poloidal flows, the Laplacian in (17) is explicitly invertable and yields an analytic description of the Coriolis pressure in terms of the Stokes Streamfunction of the poloidal flow.

c. Circularly symmetric poloidal circulation

Since the vorticity field of a circularly symmetric poloidal circulation is purely toroidal, it behooves us to compute the basis vectors in cylindrical polar coordinates as a function of angle in the plane, and express them in terms of the Cartesian basis. Clearly the vertical direction is the same in both coordinate systems, and we need only express

$$\begin{aligned} \hat{\mathbf{r}} &= \cos(\theta)\hat{\mathbf{i}} + \sin(\theta)\hat{\mathbf{j}} \\ \hat{\boldsymbol{\theta}} &= -\sin(\theta)\hat{\mathbf{i}} + \cos(\theta)\hat{\mathbf{j}}, \end{aligned} \tag{18}$$

being the axially outward, toroidal unit vectors, respectively.

Focusing on general axisymmetric, poloidal, incompressible circulations, we consider a local cylindrical coordinate system in which the velocity is written in component form as

$$\mathbf{u} = u_r(r, z)\,\hat{\mathbf{r}} + u_\theta(r, z)\,\hat{\boldsymbol{\theta}} + u_z(r, z)\,\hat{\mathbf{k}}. \tag{19}$$

The poloidal nature of the flow implies $u_\theta = 0$, and axisymmetry implies $\partial u_r/\partial\theta = \partial u_z/\partial\theta = 0$. Incompressibility of the flow in the (r, z) plane yields the nondivergent constraint for $\mathbf{u}$ in that plane:

$$\frac{1}{r}\frac{\partial (r u_r)}{\partial r} + \frac{\partial u_z}{\partial z} = 0. \tag{20}$$

Any nondivergent vector field can be expressed as the curl of a vector potential, so we can express the toroidally symmetric poloidal flow $\mathbf{u}$ as

$$\mathbf{u} = \nabla \times (\Psi \hat{\boldsymbol{\theta}}), \tag{21}$$

where $\boldsymbol{\Psi} = \Psi(r, z)\,\hat{\boldsymbol{\theta}}$ is the (nondivergent) vector potential, in analogy to the vector potential of magnetostatics. Since we will only consider poloidal circulations, and thereby toroidal vector potentials for the remainder of the discussion, hereafter we will refer to the scalar function Ψ as the vector potential (although technically it is the magnitude of the vector potential). Utilizing Ψ, the components of the poloidal velocity field are

$$u_r = -\frac{\partial \Psi}{\partial z}, \quad u_\theta = 0, \quad u_z = \frac{1}{r}\frac{\partial (r\Psi)}{\partial r}. \tag{22}$$

Although Ψ has the dimensions of a streamfunction, the flow is not tangent to contours of Ψ.

The ''Stokes streamfunction'' (Stokes 1842) is designed so that its contours are tangent to the vector field of the flow. For poloidal flows in cylindrical coordinates, the Stokes streamfunction ψ is equal to the distance from the axis multiplied by the toroidal component of the vector potential:

$$\psi = r\Psi. \tag{23}$$

Substituting (23) into (22), we find

$$\mathbf{u} = \frac{1}{r}\left[-\frac{\partial \psi}{\partial z}\hat{\mathbf{r}} + \frac{\partial \psi}{\partial r}\hat{\mathbf{k}}\right], \tag{24}$$

the velocity field is everywhere tangent to contours of ψ but proportional in magnitude to $|\nabla\psi|/r$.

The Coriolis force is computed using Ψ from (21) or (22) and the rotation vector from (10):

$$\begin{aligned} -2\boldsymbol{\Omega} \times \mathbf{u} &= -2\Omega_0[\cos(\phi)\hat{\mathbf{j}} + \sin(\phi)\hat{\mathbf{k}}] \times \left[-\frac{\partial \Psi}{\partial z}\hat{\mathbf{r}} + \frac{1}{r}\frac{\partial (r\Psi)}{\partial r}\hat{\mathbf{k}}\right] \\ &= -2\Omega_0[\cos(\phi)\sin(\theta)\hat{\mathbf{r}} + \cos(\phi)\cos(\theta)\hat{\boldsymbol{\theta}} + \sin(\phi)\hat{\mathbf{k}}] \times \left[-\frac{\partial \Psi}{\partial z}\hat{\mathbf{r}} + \frac{1}{r}\frac{\partial (r\Psi)}{\partial r}\hat{\mathbf{k}}\right] \\ &= -2\Omega_0\left\{\cos(\phi)\left[-\frac{\sin(\theta)}{r}\frac{\partial (r\Psi)}{\partial r}\hat{\boldsymbol{\theta}} + \cos(\theta)\frac{\partial \Psi}{\partial z}\hat{\mathbf{k}} + \frac{\cos(\theta)}{r}\frac{\partial (r\Psi)}{\partial r}\hat{\mathbf{r}}\right] - \sin(\phi)\frac{\partial \Psi}{\partial z}\hat{\boldsymbol{\theta}}\right\} \\ &= -2\Omega_0\left\{\cos(\phi)\left[\frac{1}{r}\frac{\partial (r\Psi)}{\partial r}\hat{\mathbf{i}} + \cos(\theta)\frac{\partial \Psi}{\partial z}\hat{\mathbf{k}}\right] - \sin(\phi)\frac{\partial \Psi}{\partial z}\hat{\boldsymbol{\theta}}\right\} \\ &= -2\Omega_0\{\cos(\phi)[u_z\hat{\mathbf{i}} - \cos(\theta)u_r\hat{\mathbf{k}}] + \sin(\phi)u_r\hat{\boldsymbol{\theta}}\}. \end{aligned} \tag{25}$$

In the last two lines of (25) we have used a cylindrical basis vector for the traditional Coriolis force [proportional to $\sin(\phi)$] and a Cartesian basis for the nontraditional Coriolis force [proportional to $\cos(\phi)$].

The last line of (25) clarifies how the Coriolis force depends on the vertical and radial components of the poloidal circulation. For the axisymmetric circulations on which we are focusing, the traditional Coriolis force is nondivergent and acts to rotate the flow about its center. It might produce, say, vortical convection or a hurricane.

As one would expect, the nontraditional force acts in the zonal and vertical directions. The x component of the velocity field is simply $u_x = \cos(\theta)u_r$ so that the NCT can be written $[u_z\hat{\mathbf{i}} - \cos(\theta)u_r\hat{\mathbf{k}}] = u_z\hat{\mathbf{i}} - u_x\hat{\mathbf{k}}$. Of course, the right-hand side of this expression is the simplest form if one wishes to focus on the total Coriolis force; however, it does not emphasize the rotational symmetry of the poloidal circulation and thereby is not useful for computing the *net* Coriolis force that arises when the pressure is computed. As we pointed out in (17), the divergence of this vector field is equal to the negative of the $\hat{\mathbf{j}}$ component of the vorticity of the poloidal circulation. Therefore, a perturbation pressure gradient will develop to compensate for the divergence of the nontraditional Coriolis force.

The $\hat{\mathbf{k}}$ component of the total Coriolis force is needed to determine the boundary condition on the Coriolis pressure. Using (25) in (16) we find

$$\frac{\partial p_C}{\partial z} = -2\Omega_0\cos(\phi)\cos(\theta)\frac{\partial \Psi}{\partial z} \quad \text{on} \quad z = 0. \tag{26}$$

The vorticity of an axisymmetric poloidal flow is purely in the toroidal direction:

$$\boldsymbol{\omega} = \left[\frac{\partial u_r}{\partial z} - \frac{\partial u_z}{\partial r}\right]\hat{\boldsymbol{\theta}}, \tag{27}$$

which, when expressed in terms of the vector potential Ψ becomes

$$\begin{aligned}\boldsymbol{\omega} &= -\left\{\frac{\partial}{\partial r}\left[\frac{1}{r}\frac{\partial(r\Psi)}{\partial r}\right] + \frac{\partial^2\Psi}{\partial z^2}\right\}\hat{\boldsymbol{\theta}} \\ &= -\left[\frac{\partial}{\partial r}\left(\frac{\partial\Psi}{\partial r} + \frac{\Psi}{r}\right) + \frac{\partial^2\Psi}{\partial z^2}\right]\hat{\boldsymbol{\theta}} \\ &= -\left[\frac{\partial^2\Psi}{\partial r^2} + \frac{1}{r}\frac{\partial\Psi}{\partial r} - \frac{\Psi}{r^2} + \frac{\partial^2\Psi}{\partial z^2}\right]\hat{\boldsymbol{\theta}}.\end{aligned} \tag{28}$$

The reader may note that $\boldsymbol{\omega} = -\nabla^2\boldsymbol{\Psi}$, the vector Laplacian of the vector potential; we could use this identity to solve for the Coriolis pressure, but we take the more brute-force approach for the sake of clarity.

Taking the dot product of the toroidal vorticity, (28), with the equation for the rotation vector, (10), yields a simple expression for the rhs of (17) for the Coriolis pressure in terms of the vector potential:

$$\begin{aligned}&\nabla^2 p_C = 2\boldsymbol{\Omega}\cdot\boldsymbol{\omega} \\ &\Rightarrow \nabla^2 p_C = -2\Omega_0\cos(\phi)\cos(\theta)\left[\frac{\partial^2\Psi}{\partial r^2} + \frac{1}{r}\frac{\partial\Psi}{\partial r} - \frac{\Psi}{r^2} + \frac{\partial^2\Psi}{\partial z^2}\right].\end{aligned} \tag{29}$$

d. Solving for the Coriolis pressure

We are left to solve (29) with the $z = 0$ boundary condition given in (26). In cylindrical coordinates, the Laplacian of the Coriolis pressure is expressed as

$$\nabla^2 p_C = \frac{\partial^2 p_C}{\partial r^2} + \frac{1}{r}\frac{\partial p_C}{\partial r} + \frac{1}{r^2}\frac{\partial^2 p_C}{\partial\theta^2} + \frac{\partial^2 p_C}{\partial z^2}. \tag{30}$$

The absolutely elegant fact is that the solution of (29) is *extremely simple*. To solve for p_C, we introduce the function $P(r, z)$ and substitute

$$p_C(r,\theta,z) = P(r,z)\cos(\theta) \tag{31}$$

into (29) using the identity from (30) to arrive at

$$\begin{aligned}&\left[\frac{\partial^2 P}{\partial r^2} + \frac{1}{r}\frac{\partial P}{\partial r} - \frac{P}{r^2} + \frac{\partial^2 P}{\partial z^2}\right]\cos(\theta) \\ &\quad = -2\Omega_0\cos(\phi)\cos(\theta)\left[\frac{\partial^2\Psi}{\partial r^2} + \frac{1}{r}\frac{\partial\Psi}{\partial r} - \frac{\Psi}{r^2} + \frac{\partial^2\Psi}{\partial z^2}\right].\end{aligned} \tag{32}$$

In general, we would have to invert the linear operator on the left hand side of this expression to solve for P–but the simplicity of this equation allows us to read off the solution without any more work. Notice that the dependence on θ and the differential operator is the same on the right and left hand sides of (32). Therefore, P is proportional to Ψ plus a yet undetermined function R. So we have found $P(r, z) = -2\Omega_0\cos(\phi)[\Psi(r, z) + R(r, z)]$, where R is a homogeneous solution of the differential operator in (32). The resulting Coriolis pressure is expressed explicitly in terms of Ψ and R as

$$p_C(r,z,\theta) = -2\Omega_0\cos(\phi)[\Psi(r,z) + R(r,z)]\cos(\theta). \tag{33}$$

Upon taking the z derivative of p_C in (33) and substituting the derivative into the boundary condition (26) we arrive at the boundary condition for R:

$$\frac{\partial R}{\partial z} = 0 \quad \text{on} \quad z = 0. \tag{34}$$

We conclude that, since R is a solution to a homogeneous elliptic partial differential equation with homogeneous boundary conditions, $R(r, z) = 0$ everywhere. Thus the Coriolis pressure, p_C, is given by the expression in (33) with $R = 0$.

e. Solving for the net Coriolis force

The negative gradient of the Coriolis pressure, (33), is

$$-\nabla p_C = 2\Omega_0\cos(\phi)\left[\frac{\partial\Psi}{\partial r}\cos(\theta)\hat{\mathbf{r}} - \frac{\Psi\sin(\theta)}{r}\hat{\boldsymbol{\theta}} + \frac{\partial\Psi}{\partial z}\cos(\theta)\hat{\mathbf{k}}\right]. \tag{35}$$

To this expression we add the Coriolis force in (25) to arrive at the net Coriolis force from (14) expressed in terms of the vector potential Ψ:

$$\begin{aligned}\mathbf{F}_{\text{net}} = 2\Omega_0\Bigg\{&-\cos(\phi)\left[\frac{\Psi}{r}\cos(\theta)\hat{\mathbf{r}} - \frac{\partial\Psi}{\partial r}\sin(\theta)\hat{\boldsymbol{\theta}}\right] \\ &+ \sin(\phi)\left[\frac{\partial\Psi}{\partial z}\hat{\boldsymbol{\theta}}\right]\Bigg\}.\end{aligned} \tag{36}$$

Notice that vertical component of the net force *vanishes everywhere* in r, θ for $z > 0$, not just at the lower boundary. This result was not obvious before we embarked upon the calculation, since the Coriolis force does have a vertical component throughout the fluid [notice the $\hat{\mathbf{k}}$ component of the force in (25)]. Nonetheless, we have shown that the component of the Coriolis force associated with the eastward component of the velocity balances the vertical gradient of the Coriolis pressure [refer to (3)], at least away from the poles where $\cos(\phi) = 0$.

The remarkably straightforward result in (36) can actually be further simplified. Using the polar coordinate representation of the curl, we can write the first term in the outermost parentheses as

$$\begin{aligned} -\left[\frac{\Psi}{r}\cos(\theta)\hat{\mathbf{r}} - \frac{\partial\Psi}{\partial r}\sin(\theta)\hat{\boldsymbol{\theta}}\right] &= \nabla\times(-\Psi(r,z)\sin(\theta)\hat{\mathbf{k}}) \\ &= \nabla\times(-G(x,y,z)\hat{\mathbf{k}}) \\ &= -\frac{\partial G}{\partial y}\hat{\mathbf{i}} + \frac{\partial G}{\partial x}\hat{\mathbf{j}} \\ &\equiv \nabla^{\perp}G, \end{aligned} \tag{37}$$

where

$$G = \Psi\sin(\theta), \tag{38}$$

and $\nabla^{\perp}$ is the perpendicular gradient, which is equivalent to the tangential derivative; $\nabla^{\perp}G$ is a vector field directed clockwise around maxima of G.

Substituting this result into the expression for the net force, (36), we arrive at the main result of our analysis:

$$\mathbf{F}_{\text{net}} = 2\Omega_0\left\{\cos(\phi)\nabla^{\perp}[\Psi\sin(\theta)] + \sin(\phi)\frac{\partial\Psi}{\partial z}\hat{\boldsymbol{\theta}}\right\}. \tag{39}$$

We interpret (39) next.

1) INTERPRETATION OF THE $\sin(\phi)$ TERM; CORIOLIS ROTATION

The second term in (39) is proportional to the sine of latitude; it vanishes at the equator, is antisymmetric about the equator, and is maximal at the poles. This term is due to the traditional Coriolis force and acts solely in the toroidal direction.

Since the force is proportional to

$$\mathbf{F}_{\text{net},2} \propto \frac{\partial\Psi}{\partial z} \propto -u_r, \tag{40}$$

we note that it is proportional to the negative of the radial velocity. This expression tells us that at elevations of maximal radial inflow, there is a maximal force in the cyclonic direction, whereas at elevations of maximal radial outflow, there is a maximal anticyclonic force. This force would tend to spin a convective cell cyclonically near the base of the troposphere and anticyclonically near the tropopause.

We name this the Coriolis rotation term. It will likely feel familiar to readers.

2) INTERPRETATION OF THE $\cos(\phi)$ TERM; CORIOLIS SHEAR

The first term in outer parenthesis in (39) is more subtle, more interesting, and in our opinion, not adequately discussed in the literature. It is symmetric about the equator, so there is no hemispheric difference in its effects. It is also maximum at the equator and vanishes at the poles.

Since it depends on the (x, y) perpendicular gradient of the function $G = \Psi\sin(\theta)$, contours of G are related to the nondivergent, net Coriolis force in the same way that a streamfunction in two dimensions is related to an incompressible velocity field. That is to say the force is tangent to contours of G, and where G changes most sharply, the force is strongest. We reiterate that, from the definition of the perpendicular gradient in (37), it is clear that the force vectors swirl counterclockwise around low values of G. Importantly, this sense of circulation of the force vectors is independent of latitude, unlike the Coriolis rotation term, whose sign changes across the equator.

We name this component of the force the "Coriolis shear" term and G [from (38)] the "shear potential." We will provide some physical insight into these next.

4. The net Coriolis force associated with the "DoNUT" model of convective circulation

An elucidating model fo a poloidal circulation is what we call the "DoNUT" Model (the "Dynamics of Nonrotating Updraft Torii"). This is a model we will introduce here and describe more completely in future work. Briefly, we imagine air flowing upward in an updraft near the "hole" of the DoNUT, air subsiding along the outer edge of the DoNUT, and a smoothly varying flow inside. For now, the simplest DoNUT is described by a vector potential that is separable in r and z (in $z \geq 0$), and independent of θ. An example of such a flow contains two length scales, L and H, and a strength, w_*:

$$\Psi(r,z) = \frac{w_*}{2}\frac{rz}{H}e^{1-z/H-2r/L}. \tag{41}$$

To understand the physical meaning of these parameters, we compute the vertical velocity:

$$\begin{aligned} u_z &= \frac{1}{r}\frac{\partial(r\Psi)}{\partial r} \\ &= w_*\frac{z}{H}\left[1-\frac{r}{L}\right]e^{1-z/H-2r/L}, \end{aligned} \tag{42}$$

and radial velocity:

$$\begin{aligned} u_r &= -\frac{\partial\Psi}{\partial z} \\ &= -\frac{w_*}{2}\frac{r}{H}\left[1-\frac{z}{H}\right]e^{1-z/H-2r/L}. \end{aligned} \tag{43}$$

Therefore, the flow described by (41) consists of a radially inward velocity below $z = H$, and a radially outward velocity above $z = H$. The maximum magnitude of the radial velocity occurs at $z = 0$ in the DoNUT, and the magnitude decreases as $r \to \infty$.

The vertical velocity is positive for $r < L$ and negative for $r > L$. The vertical velocity is maximum on the axis of symmetry,

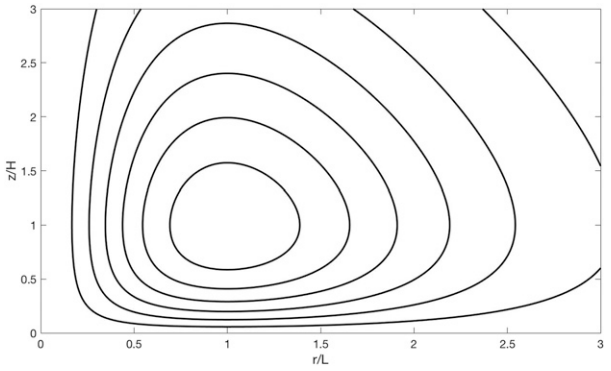

FIG. 2. Contours of the Stokes streamfunction vs $(r/L, z/H)$ for the DoNUT model of (41).

increases from the ground ($z = 0$), reaches a maximum of $u_{z,\max} = w_*$ at height $z = H$, and decreases to zero as $z \to \infty$.

In Fig. 2, we plot a radial/vertical cross section of the DoNUT's Stokes Streamfunction, $\psi = r\Psi$, in coordinates $(r/L, z/H)$. By scaling (L, H, w_*) a whole family of different flows can be described by (41). The flow shown is clockwise with its stagnation point at $(r/L = 1, z/H = 1)$.

Of the two net forces we have described, Coriolis rotation and Coriolis shear, the second is the less intuitive and is the one that needs more description. Computing the shear potential, (38), associated with the DoNUT, (41), we find

$$G(x,y,z) = \frac{w_*}{2}\frac{yz}{H}e^{1-z/H-\left(2\sqrt{x^2+y^2}\right)/L}. \tag{44}$$

We have expressed G in Cartesian coordinates since the tangential gradient, $\nabla^{\perp}$, is most easily described in Cartesian variables. The Coriolis Shear force is purely in the (x, y) plane and is derived from the (x, y) derivatives of the Shear Potential. Therefore, the z-dependent terms in the Shear Potential act together as a scale factor for the strength of the force at each height. The vertical velocity on the axis of symmetry ($r = 0$) is also the maximum velocity at each height:

$$w(z) \equiv w_*\frac{z}{H}e^{1-z/H}, \tag{45}$$

which, itself, attains the maximum w_* at $z = H$. This identification allows us to write (44) as

$$G = w(z)\frac{y}{2}e^{-\left(2\sqrt{x^2+y^2}\right)/L}. \tag{46}$$

From this expression, we learn that the maximum Coriolis shear occurs at the height of the maximum vertical velocity. In a separable streamfunction, the strength of the Coriolis shear at any height is proportional to the strength of the vertical velocity along the axis of symmetry at that height–this is the updraft velocity.

Along the axis of symmetry of the flow, the net Coriolis shear force, which is the term proportional to $\cos(\phi)$ in (39), is

$$\mathbf{F}_{\mathrm{CS}}(0,z) = -2\Omega_0\cos(\phi)\frac{\partial G}{\partial y}\hat{\mathbf{i}} = -\Omega_0\cos(\phi)\,w(z)\,\hat{\mathbf{i}}. \tag{47}$$

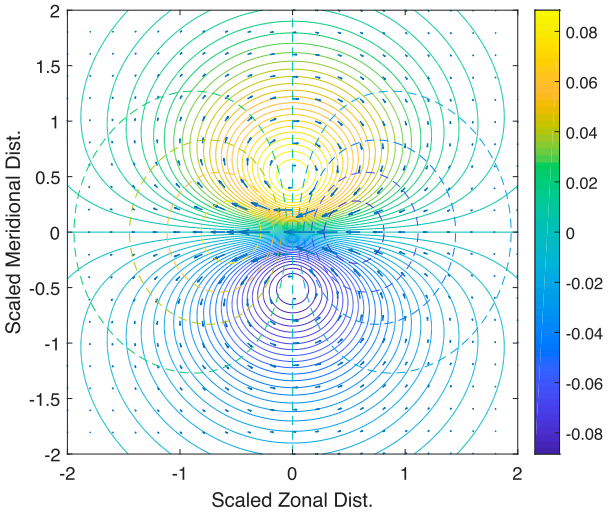

FIG. 3. The shear potential [G, solid contours, from (46)] and net Coriolis shear force vectors as a function of (x, y), divided by $w(z)$, the maximum vertical velocity at any given height. The axis scale is $(x/R, y/R)$ and the contour levels are in units of R. The dashed contours show the Coriolis pressure field.

Since the central vertical velocity is upward, the Coriolis shear force along the axis is westward and proportional in strength to the vertical velocity along the axis. Therefore, the Coriolis shear force imparts a westward tilt to convective towers and is most pronounced near the equator.

Figure 3 shows contours of G and vectors of the Coriolis shear for the DoNUT circulation at a fixed height in the troposphere. Motion is upward at the origin. The westward force at the convective core and along the latitude of the convective core is clearly visible. The lines of force also circulate as a dipole centered along the axis of symmetry. This circulating force can impart spreading throughout the convective column but is most strongly felt at the height of maximum vertical velocity. Figure 3 also shows the Coriolis pressure field. This is included to show that the meridional difluence of the net force is due to the perturbation high pressure on the down shear (i.e., western) side of the updraft.

The Coriolis shear might be visualized as a mesoscale manifestation of the synoptic tilting of meridional planetary vorticity described by Hayashi and Itoh Hayashi and Itoh (2012). In addition to tilting, the DoNUT flow is also associated with significant vertical gradients. Therefore, the Coriolis shear force also involves stretching of meridional planetary vorticity. Off the equator, the Coriolis rotation force is associated with vertical stretching of vertical planetary vorticity.

Comparing the strength of the NCT force to the inertial force due to advection

Since the time scales of rotation are much slower than those of convection, one may be left wondering how the intensity of NCT compares to that of the inertial terms in flows associated with convection, such as the DoNUT flow. Indeed, intuition and simple scaling arguments suggest the inertial terms are

often much larger than the NCT. Consider the Rossby number for a circulation of aspect ratio approximately one, where horizontal and vertical length and velocity scales are approximately the same. Using a typical velocity of $U \approx 10\,\mathrm{m\,s^{-1}}$, length scales of about $L \approx 5\,\mathrm{km}$ in the vertical direction, and a Coriolis parameter associated with the NCT at the equator of $f = 2\Omega_0 = 1.5 \times 10^{-4}\,\mathrm{s^{-1}}$, the Rossby number is

$$\mathrm{Ro} = \frac{U}{Lf} \approx 13 \tag{48}$$

meaning that, although the NCT force is smaller than the inertial force associated with the nonlinear advection term, NCT is not negligible compared to the inertial force.

Scaling arguments of this kind are meant to give a sense of the relative scales of different terms in the Euler equations, but they should not be over interpreted. At the equator, the Rossby number associated with the traditional Coriolis terms is infinite, and, therefore, it can be rigorously neglected. However, even if we have underestimated the NCT Rossby number by a factor of ten, the estimate still suggests that the NCT cannot be completely neglected.

To completely assess the relevance of the NCT, the important questions to ask are, first, how and where does the inertial force act on a convective circulation compared to the NCT force, and second, is there a systematic effect of the NCT, which is ubiquitous for convective flows in general? We have addressed this second question in section 4.

The vorticity associated with an axisymmetric poloidal circulation is purely toroidal–like smoke rings in the air. The nonlinear self-advection of this toroidal vorticity field by its own *poloidal* velocity field results in a rearrangement of the toroidal vorticity, but the vorticity remains toroidal and the resulting flow remains poloidal. Think of a smoke ring in the air, which is simply advected by its poloidal flow, but retains its shape. The details of the self-advection of a convective poloidal flow are different than a smoke ring since the convective flow exists in a stratified fluid with a rigid lower boundary. However, the basic fact remains, the nonlinear self-advection of a convective DoNUT rearranges the toroidal vorticity in a way that the vorticity remains toroidal and the velocity remains poloidal.

The axis of symmetry, where the vertical velocity is the largest, is also the axis where the vorticity is zero at all levels. Therefore it is the location within the DoNUT where the flow is least influenced by the inertial force, but most influenced by the NCT.

The effect of the NCT was also demonstrated by Eisenga et al. (1998) in elegant, laboratory and numerical experiments on vortex rings (similar to the DoNUT) in a fluid rotating along an axis perpendicular to the motion of the vortex ring. In Fig. 5 of their paper, Eisenga et al. (1998) show that, instead of traveling along the axis of symmetry, a vortex ring with a large Rossby number (=23) tilts in the opposite sense of the rotation of the fluid, tending to maintain its absolute orientation in an inertial frame of reference. These experiments are the unstratified, dynamical realization of what our analysis demonstrates kinematically—that even for large Rossby numbers, a vortex DoNUT will tilt the opposite direction of the rotation of the domain. In the atmosphere, the tilt will be westward.

5. Cloud-resolving simulations

Next, we add the NCT to the RAMS model (Cotton et al. 2003), which we run in a series of cloud-resolving configurations. These numerical simulations are intended to further our understanding of the effects of the NCT on convective clouds and to test our DoNUT model.

a. Isolated congestus simulations

We will begin with two sets of simulations run on a three-dimensional isotropic grid of 150-m spacing on a domain of 45 km on a side and 21 km tall. The simulations are initialized with a mean sounding from the DYNAMO field campaign (Ciesielski et al. 2014) with a 4% moistener boundary layer (surface to 900 hPa) to help sustain moist convection. We use the RAMS double-moment (Igel et al. 2015), bin-emulating microphysics (Saleeby and Cotton 2004; Saleeby and van den Heever 2013), cyclic lateral boundaries, 20 damping layers at model top, Mellor and Yamada Mellor and Yamada (1982) turbulence, and no radiation.

We ran six simulations. Three were run on an equatorial f plane with NCT included ($\mathrm{NCT_{on}}$) and three were run with the standard RAMS equation set ($\mathrm{NCT_{off}}$). The three simulations differed in their intensity of forced convergence in the lower atmosphere (0–3.5 km) that was included in the model to excite convection. The intensities of convergence at the surface were: 4.0×10^{-4}, 2.5×10^{-4}, and $1.5 \times 10^{-4}\,\mathrm{s^{-1}}$. We also tried $0.5 \times 10^{-4}\,\mathrm{s^{-1}}$, but it failed to excite sustained convection. The convergence intensity decreases linearly with height. We will focus on the onset of convection.

To make use of this miniensemble of large-eddy simulation (LES), we will show the ensemble, time-integrated mean of physical quantities for 20 min of simulation. All three simulations within a set are averaged together to best ensure results are general and not just the result of numerical noise. Figures 4a and 4b show the ensemble-mean zonal and vertical winds. These figures show the wind is convergent at the surface and convective from just above the surface to at least 4 km. Figures 4c and 4d show differences of these quantities between the two simulations (taken as $\mathrm{NCT_{on}}$ minus $\mathrm{NCT_{off}}$). These difference plots show two results that are not necessarily obvious from examining (1) and (3). First, zonal wind differences are predominantly negative at the surface and positive in the core of the updraft. Second, there is a coherent, though somewhat noisy, velocity couplet in the vertical wind difference.

We take these noted differences to be simulated examples of the symmetry breaking discussed in section 2a. The negative zonal velocity difference at the surface may be the result of preferential lifting of parcels with positive zonal velocities and preferential sinking (in this case, to the ground) of parcels with negative zonal momentum. The positive zonal momentum near 2 km results from the preferential lifting of westerly surface air. Figure 4d illustrates the impact of (3); air with positive zonal momentum has higher vertical velocity up to about 3-km

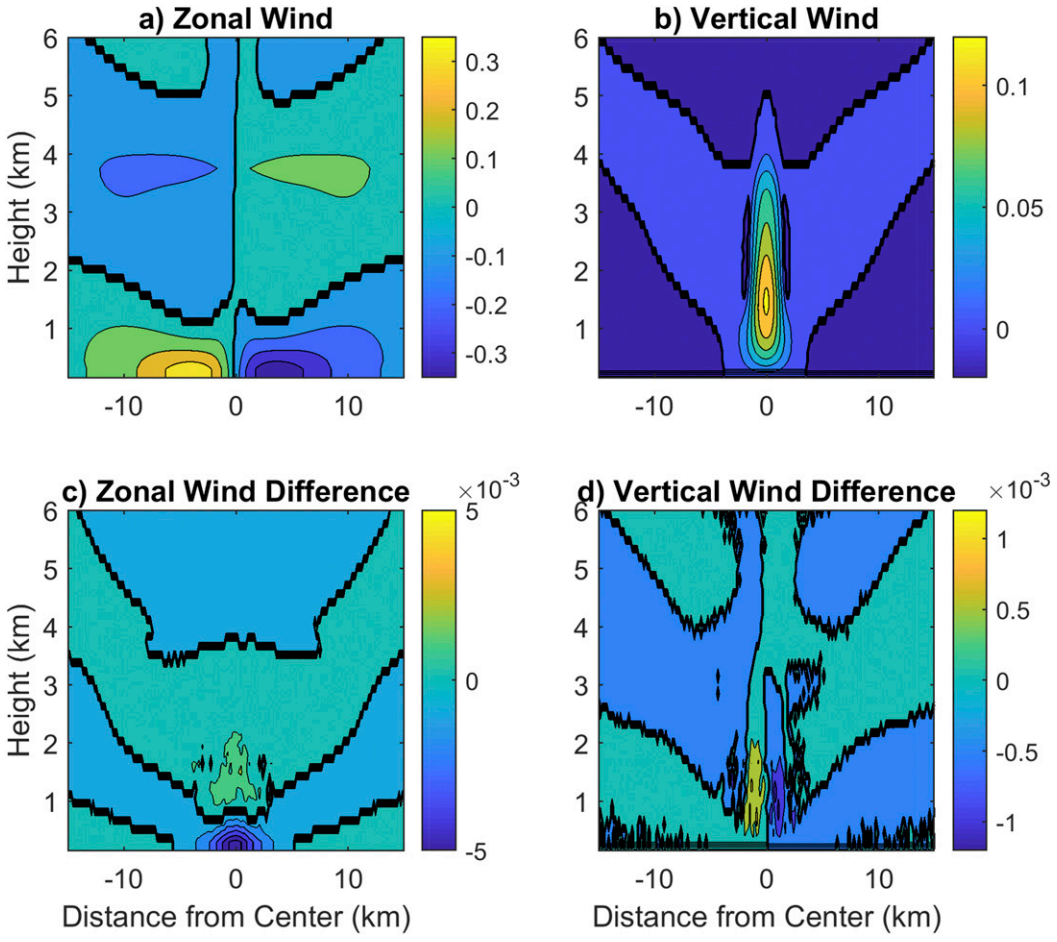

FIG. 4. Vertical cross sections of velocity (in NCT_{on}) and velocity differences (as NCT_{on} minus NCT_{off}). (a) Zonal velocity through the convergence center in NCT_{on}. (b) Vertical velocity in NCT_{on}. (c) Zonal velocity enhancement in NCT_{on}. (d) Vertical velocity enhancement in NCT_{on}.

height. The maximum magnitude of the velocity differences is approximately 1% of the magnitude of the composite velocities. While the effect of the NCT on short-lived convection appears to be weak, we want to stress that it is systematic although, of course, this theory is developed with simple parcel thinking.

The positive/negative vertical velocity couplet around $x = 0$ in Fig. 4d comes about because the core of the vertical wind has been forced to the west at altitudes of maximum zonal wind in the NCT_{on} experiments. The vertical velocity difference basically integrates horizontally to zero at every vertical level. Such a function describes a westward shift in the vertical velocity between the NCT_{off} and NCT_{on} experiments. Furthermore the vertical velocity difference is maximally positive (or negative) at 1.5-km height, where the vertical wind is maximal. Both the westward shift in the location of the core of the vertical velocity, and the fact that shift is itself maximal at heights of maximum vertical velocity, are predicted by our calculation of the net NCT in (47).

b. *Radiative convective equilibrium simulations*

We also ran two sets of radiative convective equilibrium (RCE) simulations. New simulations were run starting after day 60 of the RCE simulations from Igel and Igel (2018) without hydrometeor friction. The original simulation was initialized with random perturbations to the temperature and moisture fields and was then run over a fixed surface temperature ocean at 301 K with diurnally varying shortwave. Here, we added an additional 10 days of simulation. RAMS was run with a 200-km square, doubly periodic domain with 1-km spacing and 65 vertical levels with stretched spacing (see Fig. 5). At the time of the restart, all the RAMS thermodynamic variables, including hydrometeor species, were used to initialize the new run but the dynamic fields were universally set to zero. We reset the dynamic fields to eliminate the imprint of any mean flow that may have developed in the 60-day run. It did not take long for the simulation to spin up new kinetic energy similar to the behavior seen in Colin et al. (2019). We ran two simulations, RCE_{on} and RCE_{off}, where "on" and "off" refer to the NCT. We show results averaged over the final 5 days of these simulations.

Figure 5a shows the average convective vertical velocity conditioned on a minimum of 1 m s^{-1}. Unlike in the LES, the RCE statistics indicate weaker convective strength throughout

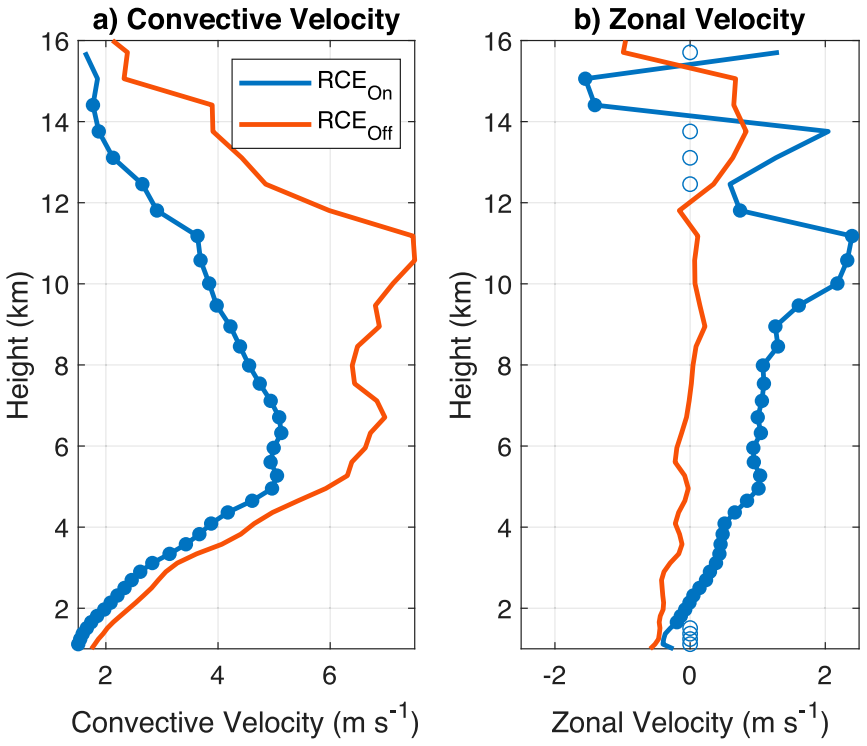

FIG. 5. Profiles of mean (a) convective (i.e., $>1\,\mathrm{m\,s^{-1}}$) vertical velocity and (b) zonal velocity in convection in $\mathrm{RCE_{on}}$ and $\mathrm{RCE_{off}}$. Filled circles indicate model levels where the statistical distributions of convective respective velocities are distinguishable from one another by a two-sided *t* test at the 99% level.

the depth of the convecting layer. The magnitude of the difference is surprisingly large especially given the result above that the Coriolis Shear has no vertical component. It averages approximately $2\,\mathrm{m\,s^{-1}}$ above the freezing level (at 5 km). The structural difference in the velocity profile is the height of the maximum. In $\mathrm{RCE_{on}}$, the maximum vertical velocity occurs at around 6 km; in $\mathrm{RCE_{off}}$, there is a local maximum near the same altitude but the global maximum occurs much higher at around 11 km. Solid dots are included in Fig. 5a to indicate levels at which vertical velocity distributions in $\mathrm{RCE_{on}}$ and $\mathrm{RCE_{off}}$ are statistically different as determined by a two-sided *t* test at the 99% level. Convective vertical wind distributions are distinguishable at every level below 15 km.

In Fig. 5b, we show the profile of mean zonal velocity in convecting grid boxes. We see a clear preference for convection to occur in locations with positive zonal velocity. The figure also indicates that convection occurs in more highly sheared environments in $\mathrm{RCE_{on}}$ (at least statistically), which, all else being equal, would tend to weaken convective intensity. To fully explain the differences in shear, we would need to track and analyze the convective and subsident momentum transport throughout the simulations. This could be a useful exercise in future work.

Next, we contrast the nature of precipitation in $\mathrm{RCE_{on}}$ with $\mathrm{RCE_{off}}$. We do this by constructing composite surface precipitation intensity maps from the instantaneous output from RAMS. Maps are constructed so that the maximum precipitation value occurring within a contiguous region of precipitation intensity greater than or equal to $1\,\mathrm{mm\,h^{-1}}$ occurs in its middle. All precipitation values outside this region are zeroed. Because of the doubly periodic nature of the RCE simulations, maps are padded out on all sides and then pared back to the size of the simulation grid (200 km × 200 km) centered on the precipitation maximum.

Figure 6 shows the azimuthally averaged, event-mean structure of precipitation intensity. In $\mathrm{RCE_{off}}$, maximum mean precipitation falls at approximately $15\,\mathrm{mm\,h^{-1}}$ while in $\mathrm{RCE_{on}}$, the maximum intensity is only $12\,\mathrm{mm\,h^{-1}}$. This could simply be a consequence of the decrease in maximum updraft speeds (Fig. 5). Or, it could be due to a change in the structure of clouds. Figure 6 shows that while the peak intensity of composite precipitation in $\mathrm{RCE_{on}}$ is lower, rain rates are actually higher beyond 10 km from the composite center. The right axis of Fig. 6 helps to show the importance of this difference. It indicates the azimuthal accumulation of rainfall (essentially just a distance weighting to the mean). The peak accumulation occurs 5 km from the composite storm centers and is 25% higher in $\mathrm{RCE_{off}}$. But beyond 12 km, $\mathrm{RCE_{on}}$ storms have as much as 300% more accumulation (due to small accumulation in $\mathrm{RCE_{off}}$). That is, precipitation features are much wider in $\mathrm{RCE_{on}}$. An approximate visual integration of the red curves indicates the total precipitation accumulation in the composite storm in $\mathrm{RCE_{off}}$ and $\mathrm{RCE_{on}}$ are nearly

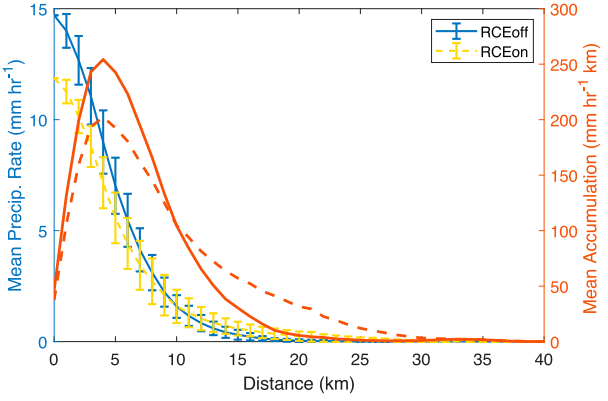

FIG. 6. The axisymmetrized composite of precipitation intensity (blue and gold) and the axial accumulated precipitation (red). Error bounds are the standard deviation of 60 samples in RCE_{off} and 44 in RCE_{on}.

the same (the difference is, indeed, within 1%). The implied lateral spreading of precipitation is consistent with an increase in the shear of convective environments.

c. *Simulating the DoNUT*

Finally, we are left wondering whether we can recreate the DoNUT with more RAMS simulations. The DoNUT model is steady state. To reflect this, we ran a set of RAMS simulations with a surface enthalpy flux that varies in space only but with an otherwise identical setup to the RAMS LES. The flux occurs over a double-Gaussian patch in the center of the domain with a full width at half maximum of 10 km. The maximum flux is 500 W m^{-2}. Microphysics is turned off for simplicity. The two simulations are $DONUT_{off}$ and $DONUT_{on}$. They are run for 3 h to approximate the time scale of sustained convection. An ascending plume sets up over the enthalpy flux patch while the rest of the domain is characterized by far-field descent. The flow characteristics of the convective circulation in $DONUT_{on}$ can be seen in Figs. 7a and 7c. The flows shown have been averaged horizontally (in Figs. 7a,b) over the middle 5 km and vertically (in Figs. 7c,d) between 3.8- and 5.6-km height (i.e., just above the level of maximum vertical wind speed) and over the final 30 min of the simulations.

Figures 7b and 7d show the differences in the flow in the vertical and horizontal planes ($DONUT_{on}$ minus $DONUT_{off}$). Figure 7b illustrates the induced cyclonic rotation (viewed from the south) in the vertical plane. While we cannot calculate the force from the model in a way that would be identical to the DoNUT model, we can instead show the resulting flow which proves to be remarkably consistent with that implied by the force in Fig. 3. RAMS simulates westward acceleration (as it does in NCT_{on} and RCE_{on}) and the meridional confluence and difluence pattern predicted by the DoNUT model. This pattern is reflective of what is shown at the synoptic scale for a simulated hurricane in Liang and Chan (2005) (their Fig. 7), although here with a much more prominent closed circulation due to the single updraft maximum. But the cause and effect are the same: a central region of uplift forces anticyclonic vorticity to the north and cyclonic vorticity to the south through the NCT.

6. Summary

In some sense, the question we have asked has an obvious answer: might equatorial deep convective clouds feel an effect from the Nontraditional Coriolis Terms (NCT)? Intuition may suggest that the answer is "no" given subdaily time scales of convection. Perhaps surprisingly, then, we have shown that the answer is more likely "yes." Taken as a whole, why do we suggest this?

We discussed a simple, Lagrangian scaling argument that depends on the relatively weak 10 m s^{-1} updrafts in tropical convection and relatively deep convective layer of 18 km results in a 2.4-km zonal displacement of an isolated ascending parcel. This suggests that convective plumes should tilt systematically to the west at 7.5° relative to the vertical. Westward tilts occur on either side of the equator and are maximal at the equator. But such a scaling ignores important aspects of convection in the atmosphere. So, we introduced a poloidal model of convection (manifest in the "DoNUT" model) to characterize the entire convective circulation that links fast convective processes with slow compensating decent.

To our poloidal idealization of convection, we applied the Leray projection in order to diagnose the pressure field. This allowed us to describe the complete Coriolis force acting on a convective flow. We briefly described two forces imposed by Earth's rotation. One we called the Coriolis rotation term that depends on the sine of latitude (and the familiar Coriolis terms), and the other, we called Coriolis shear. The latter derives from the NCT and results in tilting of convective ascent and anomalous poleward flow to the west and equatorward flow to the east.

To illustrate the impact of our simple mathematical arguments, we added the NCT to RAMS and ran three groups of simulations. The first was a small ensemble of congestus simulations. The impact of the NCT was to preferentially lift air with positive zonal momentum and to shift updrafts westward. The second was a set of restarted RCE simulations. There, we showed that (in a statistical sense) convective velocities are weakened and contiguous precipitating regions are widened by the NCT. The third was of steady-state convection due to a patch of high surface enthalpy flux. The NCT resulted in a tilted overturning structure in the vertical plane and the confluence-difluence couplet suggested by our DoNUT model in the horizontal plane.

As a practical suggestion, we think it is reasonable to include the NCT in cloud-resolving models. That is not to say it should be used in all simulations just as the traditional terms are often excluded intentionally in simulations. We would also suggest that systematic tilts to convective storms, of the sort suggested above, could be observable in vertically resolved cloud data if suitably shear-free conditions can be found. Unfortunately, current satellite instruments are locked in predominantly north–south orbits, which would largely preclude their providing useful observation.

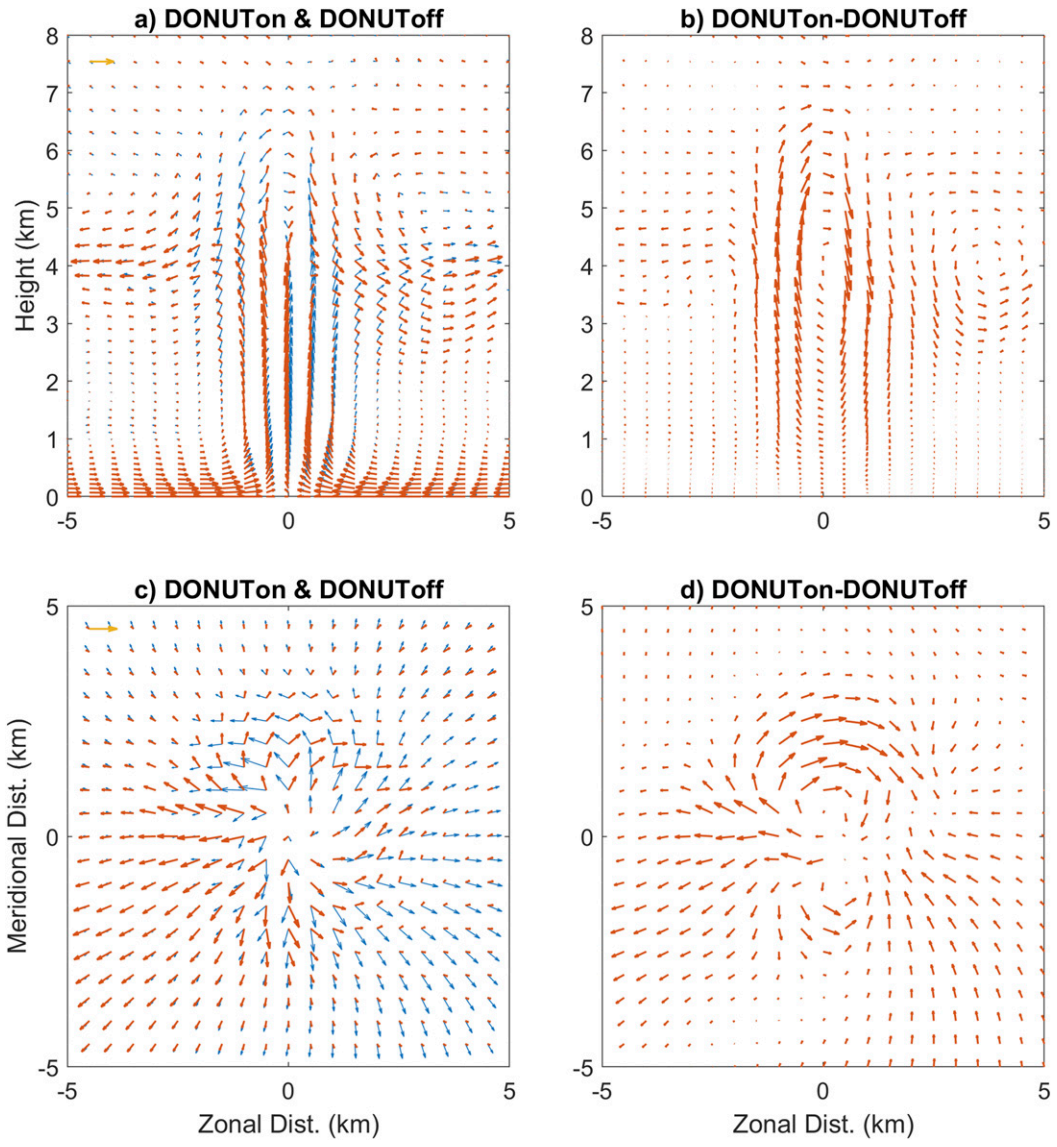

FIG. 7. Mean flows for the DONUT simulations. (a),(b) Zonal–vertical cross sections along the axis of convergence averaged over 5 km into and out of the page. (c),(d) Horizontal cross sections averaged between 3.8 and 5.6 km above the surface. (a),(c) The flow in DONUT_{on} (overlain in red) and $\text{DONUT}_{\text{off}}$ (underlain in blue). Yellow vectors illustrate a magnitude of 9 m s^{-1}, which is approximately the largest magnitude vector in each panel.

Acknowledgments. MRI would like to thank his recent ATM121A classes who dealt with the NCT on various exams. MRI would also like to acknowledge startup funding from the University of California Davis. MRI and JAB would like to thank Dr. Hing Ong and two additional reviewers. MRI and JAB conceived the work. MRI ran and analyzed simulations. JAB performed the mathematically analysis. MRI and JAB wrote the manuscript. JAB would like to dedicate his effort in this work to the memory of Dr. René Samson, formerly of M.I.T. and the Shell Corporation. René's mathematical insights, impeccable mathematical and artistic taste, and his drive for understanding made him a great Renaissance man and an inspiration to those who met him.

Data availability statement. Data used in figures are available at https://doi.org/10.25338/B8J61W.

REFERENCES

Bryan, G. H., and J. M. Fritsch, 2002: A benchmark simulation for moist nonhydrostatic numerical models. *Mon. Wea. Rev.*, **130**, 2917–2928, https://doi.org/10.1175/1520-0493(2002)130<2917:ABSFMN>2.0.CO;2.

Busse, F., 1976: A simple model of convection in the Jovian atmosphere. *Icarus*, **29**, 255–260, https://doi.org/10.1016/0019-1035(76)90053-1.

Ciesielski, P. E., and Coauthors, 2014: Quality-controlled upper-air sounding dataset for DYNAMO/CINDY/AMIE: Development

and corrections. *J. Atmos. Oceanic Technol.*, **31**, 741–764, https://doi.org/10.1175/JTECH-D-13-00165.1.

Colin, M., S. Sherwood, O. Geoffroy, S. Bony, and D. Fuchs, 2019: Identifying the sources of convective memory in cloud-resolving simulations. *J. Atmos. Sci.*, **76**, 947–962, https://doi.org/10.1175/JAS-D-18-0036.1.

Cotton, W. R., and Coauthors, 2003: RAMS 2001: Current status and future directions. *Meteor. Atmos. Phys.*, **82**, 5–29, https://doi.org/10.1007/s00703-001-0584-9.

de Coriolis, G.-G., 1835: Memoire sur les equations du mouvement relatif des systemes de corps. *J. Ecol. Polytech.*, **XXIV**, 142–154.

Denbo, D. W., and E. D. Skyllingstad, 1996: An ocean large-eddy simulation model with application to deep convection in the Greenland Sea. *J. Geophys. Res.*, **101**, 1095–1110, https://doi.org/10.1029/95JC02828.

Dintrans, B., M. Rieutord, and L. Valdettaro, 1999: Gravito-inertial waves in a rotating stratified sphere or spherical shell. *J. Fluid Mech.*, **398**, 271–297, https://doi.org/10.1017/S0022112099006308.

Eisenga, A., R. Verzicco, and G. van Heijst, 1998: Dynamics of a vortex ring moving perpendicularly to the axis of a rotating fluid. *J. Fluid Mech.*, **354**, 69–100, https://doi.org/10.1017/S0022112097007702.

Gerkema, T., J. T. Zimmerman, L. R. Maas, and H. Van Haren, 2008: Geophysical and astrophysical fluid dynamics beyond the traditional approximation. *Rev. Geophys.*, **46**, RG2004, https://doi.org/10.1029/2006RG000220.

Hayashi, M., and H. Itoh, 2012: The importance of the nontraditional Coriolis terms in large-scale motions in the tropics forced by prescribed cumulus heating. *J. Atmos. Sci.*, **69**, 2699–2716, https://doi.org/10.1175/JAS-D-11-0334.1.

Igel, A. L., M. R. Igel, and S. C. van den Heever, 2015: Make it a double? Sobering results from simulations using single-moment microphysics schemes. *J. Atmos. Sci.*, **72**, 910–925, https://doi.org/10.1175/JAS-D-14-0107.1.

Igel, M. R., and A. L. Igel, 2018: The energetics and magnitude of hydrometeor friction in clouds. *J. Atmos. Sci.*, **75**, 1343–1350, https://doi.org/10.1175/JAS-D-17-0285.1.

Kasahara, A., 2003: On the nonhydrostatic atmospheric models with inclusion of the horizontal component of the earth's angular velocity. *J. Meteor. Soc. Japan*, **81**, 935–950, https://doi.org/10.2151/jmsj.81.935.

LeMone, M. A., 1983: Momentum transport by a line of cumulonimbus. *J. Atmos. Sci.*, **40**, 1815–1834, https://doi.org/10.1175/1520-0469(1983)040<1815:MTBALO>2.0.CO;2.

Liang, X., and J. C. L. Chan, 2005: The effects of the full Coriolis force on the structure and motion of a tropical cyclone. Part I: Effects due to vertical motion. *J. Atmos. Sci.*, **62**, 3825–3830, https://doi.org/10.1175/JAS3545.1.

Marshall, J., and F. Schott, 1999: Open-ocean convection: Observations, theory, and models. *Rev. Geophys.*, **37**, 1–64, https://doi.org/10.1029/98RG02739.

Mellor, G., and T. Yamada, 1982: Development of a turbulence closure model for geophysical fluid problems. *Rev. Geophys. Space Phys.*, **20**, 851, https://doi.org/10.1029/RG020i004p00851.

Ogilvie, G. I., and D. N. C. Lin, 2004: Tidal dissipation in rotating giant planets. *Astrophys. J.*, **610**, 477–509, https://doi.org/10.1086/421454.

Ong, H., and P. E. Roundy, 2019: Linear effects of nontraditional Coriolis terms on intertropical convergence zone forced large-scale flow. *Quart. J. Roy. Meteor. Soc.*, **145**, 2445–2453, https://doi.org/10.1002/qj.3572.

——, and ——, 2020: Nontraditional hypsometric equation. *Quart. J. Roy. Meteor. Soc.*, **146**, 700–706, https://doi.org/10.1002/qj.3703.

Poisson, S. D., 1838: Sur le mouvement des Projectiles dans l'air, en ayant egard a la rotation de le terre. *J. Ecol. Polytech.*, **xvi**, 1–226.

Saleeby, S. M., and W. R. Cotton, 2004: A large-droplet mode and prognostic number concentration of cloud droplets in the Colorado State University Regional Atmospheric Modeling System (RAMS). Part I: Module descriptions and supercell test simulations. *J. Appl. Meteor.*, **43**, 182–195, https://doi.org/10.1175/1520-0450(2004)043<0182:ALMAPN>2.0.CO;2.

——, and ——, 2008: A binned approach to cloud-droplet riming implemented in a bulk microphysics model. *J. Appl. Meteor. Climatol.*, **47**, 694–703, https://doi.org/10.1175/2007JAMC1664.1.

——, and S. C. van den Heever, 2013: Developments in the CSU-RAMS aerosol model: Emissions, nucleation, regeneration, deposition, and radiation. *J. Appl. Meteor. Climatol.*, **52**, 2601–2622, https://doi.org/10.1175/JAMC-D-12-0312.1.

Satoh, M., T. Matsuno, H. Tomita, H. Miura, T. Nasuno, and S. Iga, 2010: Nonhydrostatic Icosahedral Atmospheric Model (NICAM) for global cloud resolving simulations. *J. Comput. Phys.*, **115**, D00H14, http://doi.org/10.1029/2009JD012247.

Savonije, G. J., and J. C. B. Papaloizou, 1997: Non-adiabatic tidal forcing of a massive, uniformly rotating star—II. The low-frequency, inertial regime. *Mon. Not. Roy. Astron. Soc.*, **291**, 633–650, http://doi.org/10.1093/mnras/291.4.633.

Skamarock, W. C., and Coauthors, 2008: A description of the Advanced Research WRF version 3. NCAR Tech. Note NCAR/TN-475+STR, 113 pp., https://doi.org/10.5065/D68S4MVH.

Stokes, G., 1842: On the steady motion of incompressible fluids. *Trans. Cambridge Philos. Soc.*, **7**, 439–453.

Tort, M., and T. Dubos, 2014: Dynamically consistent shallow-atmosphere equations with a complete Coriolis force. *Quart. J. Roy. Meteor. Soc.*, **140**, 2388–2392, https://doi.org/10.1002/qj.2274.